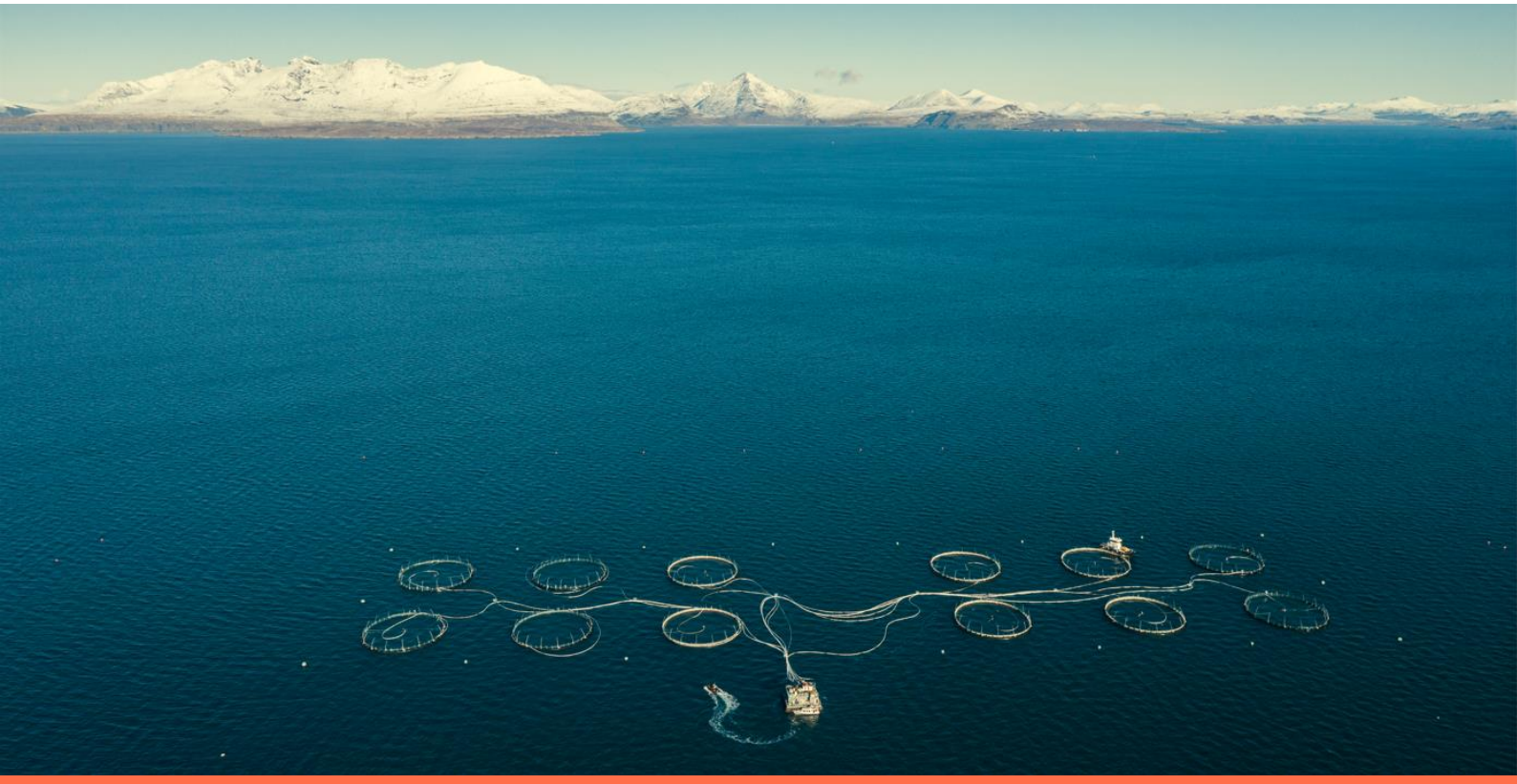

Hydrodynamic Model Description

Caol Mor, Sound of Raasay

CAR/L/1010432/C1/V4 (Cairidh)

CAR/L/1009643/C1/V4 (Maol Ban)

CAR/L/1157209 (Sconser Quarry)

January 2022

[redacted]

CONTENTS

		Page
1.	MODEL DESCRIPTION	4
2.	CONFIGURATION AND BOUNDARY FORCING FOR CAOL MOR	5
3.	MODEL CALIBRATION AND VALIDATION	8
3.1	Calibration: 5th December 2016 – 6th February 2017 (ID132)	9
3.2	Validation: 17th April – 8th July 2020 (ID339)	12
3.3	Validation: 5th July – 20th September 2018 (ID230, Maol Ban)	15
3.4	Validation: 22nd September – 2nd December 2020 (ID360, Cairidh)	17
4.	MODELLED FLOW FIELDS	20
5.	REFERENCES	21

LIST OF FIGURES

Figure 1. The mesh and domain of the East Coast of Lewis and Harris (ECLH) sub-model of the Scottish Shelf Model (Marine Scotland, 2016). 6

Figure 2. The unstructured mesh around the Caol Mor area containing three active Mowi farm sites (●): Caridh, Maol ban and Sconser Quarry. The modelled local river discharge locations are indicated (→). 6

Figure 3. Model water depths, H (m), in the area around the Caol Mor salmon farms. 7

Figure 4. Annual climatological river flows into Loch Ainort and Loch Sligachan used in the modelling. 8

Figure 5. Locations of the ADCP deployments relative to the three farms at Caol Mor. 9

Figure 6. Comparison between observed and modelled sea surface height from December 2016 – February 2017 (ADCP deployment ID132) using model parameter values from Table 1. Both the full record (left) and a subset of 15 days (right) are shown. Observed data are in blue, model results in red. 10

Figure 7. Comparison between observed and modelled East (left) and North (right) components of velocity at the ADCP location for 15 days in December 2016 – February 2017 (ID132) at two depths, 7m (top) and 17m (bottom). Observed data are in blue, model results in red. 11

Figure 8. Scatter plot of observed and modelled velocity at the ADCP location from December 2016 – February 2017 (ID132) at two depths, 7m (top) and 17m (bottom). Observed data are in blue, model results in red. 11

Figure 9. Histograms of observed and modelled speed (left) and direction (right) at the ADCP location from December 2016 – February 2017 (ID132) at two depths, 7m (top) and 17m (bottom). Observed data are in blue, model results in red. 12

Figure 10. Comparison between observed and modelled sea surface height from April – July 2019 (ADCP deployment ID339) using model parameter values from Table 1. Both the full record (left) and a subset of 15 days (right) are shown. Observed data are in blue, model results in red. 13

Figure 11. Comparison between observed and modelled East (left) and North (right) components of velocity at the ADCP location for 15 days in April – July 2020 (ID339) at two depths, 6.9 m (top) and 16.9 m (bottom). Observed data are in blue, model results in red. 13

Figure 12. Scatter plot of observed and modelled velocity at the ADCP location from April – July 2020 (ID339) at two depths, 6.9m (top) and 16.9 m (bottom). Observed data are in blue, model results in red. 14
Figure 13. Histograms of observed and modelled current speed (left) and direction (right) at the ADCP location from April – July 2020 (ID339) at two depths, 6.9m and 16.9m (bottom). Observed data are in blue, model results in red. 14
Figure 14. Comparison between observed and modelled sea surface height from July – September 2018 (ADCP deployment ID230) using model parameter values from Table 1. Both the full record (left) and a subset of 15 days (right) are shown. Observed data are in blue, model results in red. 15
Figure 15. Comparison between observed and modelled East (left) and North (right) components of velocity at the ADCP location for 15 days in July 2018 (ID230) at two depths, 8.9m (top) and 15.9m (bottom). Observed data are in blue, model results in red. 16
Figure 16. Scatter plot of observed and modelled velocity at the ADCP location from July – September 2018 (ID230) at two depths, 8.9m (top) and 15.9m (bottom). Observed data are in blue, model results in red. 16
Figure 17. Histograms of observed and modelled current speed (left) and direction (right) at the ADCP location from July – September 2018 (ID230) at two depths, 8.9m (top) and 15.9m (bottom). Observed data are in blue, model results in red. 17
Figure 18. Comparison between observed and modelled sea surface height from September – December 2020 (ID360) using model parameter values from Table 1. Both the full record (left) and a subset of 15 days (right) are shown. Observed data are in blue, model results in red. 18
Figure 19. Comparison between observed and modelled East (left) and North (right) components of velocity at the ADCP location for 15 days in September – October 2020 (ID360) at two depths, 5.9m (top) and 15.9m (bottom). Observed data are in blue, model results in red. 18
Figure 20. Scatter plot of observed and modelled velocity at the ADCP location from September – December 2020 (ID360). Observed data are in blue, model results in red. 19
Figure 21. Histograms of observed and modelled speed (left) and direction (right) at the ADCP location from September – December 2020 (ID360) at two depths, 5.9m (top) and 15.9m (bottom). Observed data are in blue, model results in red. 19

Figure 22. Modelled flood (left) and ebb (right) surface current vectors during spring tides on 7th May 2020. For clarity, only 25% of the model vectors are shown. 20
Figure 23. Modelled flood (left) and ebb (right) surface current vectors during neap tides on 14th May 2020. For clarity, only 25% of the model vectors are shown. 20

LIST OF TABLES

Table 1. Parameter values chosen for the RiCOM model during the calibration simulations.. 9
Table 2. Model performance statistics for sea surface height (SSH) and East and North velocity at the ADCP location from December 2016 – February 2017 (ID132) at two depths (7m and 17m). 10
Table 3. Model performance statistics for sea surface height (SSH), and East and North velocity at the ADCP location from April – July 2020 (ID339) at two depths, 6.9m and 16.9m. 12
Table 4. Model performance statistics for sea surface height (SSH), and East and North velocity at the Maol Ban ADCP location from the calibration simulation, July – September 2018 (ID230) at two depths, 8.9m and 15.9m.....15
Table 5. Model performance statistics for sea surface height (SSH), and East and North velocity at the ADCP location from September – December 2020 (ID360) at two depths, 5.9m and 15.9m. 17

1. Model Description

The hydrodynamic model used in the Sconser Quarry bath medicine dispersion modelling report (Mowi Scotland Ltd., 2022) was RiCOM (River and Coastal Ocean Model), a general-purpose hydrodynamics and transport model, which solves the standard Reynolds-averaged Navier-Stokes equation (RANS) and the incompressibility condition, applying the hydrostatic and Boussinesq approximations. It has been tested on a variety of benchmarks against both analytical and experimental data sets (e.g. Walters & Casulli 1998; Walters 2005a, b). The model has been previously used to investigate the inundation risk from tsunamis and storm surge on the New Zealand coastline (Walters 2005a; Gillibrand et al. 2011; Lane et al. 2011), to study tidal currents in high energy tidal environments (Walters et al. 2010) and, more recently, to study tidal energy resource (Plew & Stevens 2013; Walters et al. 2013; Walters 2016) and the effects of energy extraction on the ambient environment (McIlvenny et al. 2016; Gillibrand et al. 2016).

The basic equations considered here are the three-dimensional (3D) shallow water equations, derived from the Reynolds-averaged Navier-Stokes equations by using the hydrostatic assumption and the Boussinesq approximation. The continuity equation for incompressible flows is:

$$\nabla \cdot u + \frac{\partial w}{\partial z} = 0 \tag{1}$$

where **u**(x,y,z,t) is the horizontal velocity vector, w(x,y,z,t) is the vertical velocity, ∇ is the horizontal gradient operator, and z is the vertical coordinate. The momentum equation in non-conservative form is given by:

$$\frac{Du}{Dt} + f\hat{z} \times u + \frac{1}{\rho_0}\nabla p - \frac{\partial}{\partial z}\left(A_V \frac{\partial u}{\partial z}\right) - \nabla \cdot (A_h \nabla u) + F = 0 \tag{2}$$

where t is time; f(x,y) is the Coriolis parameter; $\hat{z}$ is the upward unit vector; p(x,y,z,t) is pressure; ρ_0 is a reference density; A_V(x,y,z,t) and A_h(x,y,z,t) are the vertical and horizontal eddy viscosities respectively; **F** represents body forces including form drag from obstacles in the flow; and x, y are the horizontal coordinates aligned to the east and north respectively.

The free surface equation is formed by vertically integrating the continuity equation and applying the kinematic free surface and bottom boundary conditions:

$$\frac{\partial \eta}{\partial t} - \nabla \cdot \left(\int_{-H}^{\eta} u dz\right) = 0 \tag{3}$$

where H is the water depth relative to the mean level of the sea.

The model can be run in two- or three-dimensional mode. Frictional stress, $\boldsymbol{\tau}_b$, is applied at the seabed as a quadratic function of velocity:

$$\tau_b = \rho C_D U_b |U_b| \tag{4}$$

where ρ = 1025 kg m^{-3} is the water density. The velocity, U_b, is either the velocity at the lowest sigma layer if the model is run in 3D or the depth-averaged velocity if run in 2D. The drag coefficient, C_D, can be either a constant or calculated from the bed roughness lengthscale, z_0, using:

$$C_D = \left(\frac{\kappa}{\ln\left((z_b+z_0)/z_0\right)}\right)^2 \quad (5)$$

where κ=0.4 is von Karman's constant, and z_b is the height above the bed of the lowest velocity point.

Wind forcing was applied as a surface stress calculated from hourly wind speed and direction. Wind stress was calculated from the wind velocity by a standard quadratic relation:

$$\tau_x = \rho_a C_S u W \quad (6a)$$
$$\tau_y = \rho_a C_S v W \quad (6b)$$

where (u,v) are the East and North components of wind velocity respectively, W is the wind speed ($W = [u^2+v^2]^{½}$), ρ_a is the density of air, and the surface drag coefficient C_S is calculated following Wu (1982) or Large and Pond (1981).

The equations are discretized on an unstructured grid of triangular elements which permits greater resolution of complex coastlines. The momentum and free surface equations are solved using semi-implicit techniques to optimize solution time and avoid the CFL stability constraint (Walters 2016). The material derivative in (2) is discretized using semi-Lagrangian methods to remove stability constraints on advection (Casulli, 1987; Walters et al. 2008). The Coriolis term is solved using a 3rd order Adams-Bashforth method (Walters et al. 2009). Full details of the model discretization and solution methods can be found in Walters et al. (2013) and Walters (2016). The solution methods provide a fast, accurate and robust code that runs efficiently on multi-core desktop workstations with shared memory using OpenMP. Full details of the model discretization and solution methods, including the basis of the application to tidal energy, are given by Walters et al. (2013) and Walters (2016).

2. Configuration and Boundary Forcing for Caol Mor

The unstructured mesh used in the model was adapted from East Coast of Lewis and Harris (ECLH) sub-model mesh (Figure 1) of the Scottish Shelf Model (SSM; MS, 2016). Model resolution was enhanced in the Sound of Raasay region particularly around the Mowi sites (Figure 2). The spatial resolution of the model varied from 25m in some inshore waters to 5 km along the open boundary. In total, the model consisted of 44,600 nodes and 83,538 triangular elements.

Water depths in the model were based on the original ECLH model, but were modified in the Sound of Raasay area using bathymetry from the UK Hydrographic Office portal (UKHO 2022), which contains high resolution data in the inshore waters around the islands of Raasay and Scalpay. These data were interpolated onto the node locations in Sound of Raasay region around the farm sites (Figure 3).

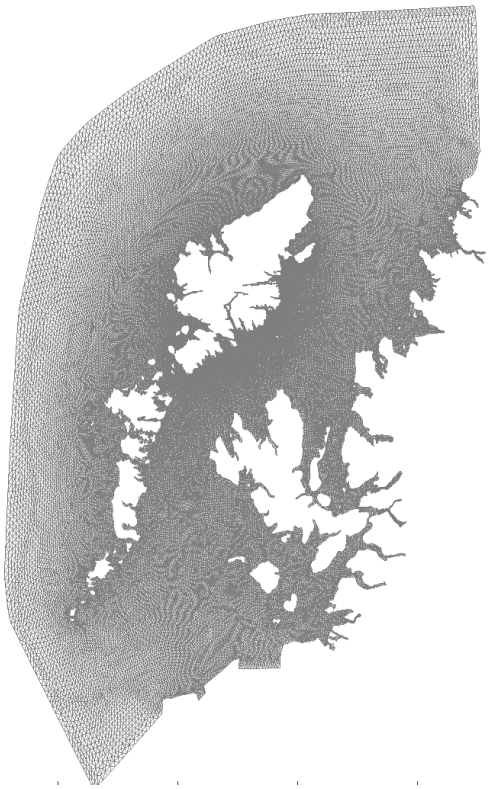

Figure 1. The mesh and domain of the East Coast of Lewis and Harris (ECLH) sub-model of the Scottish Shelf Model (Marine Scotland, 2016).

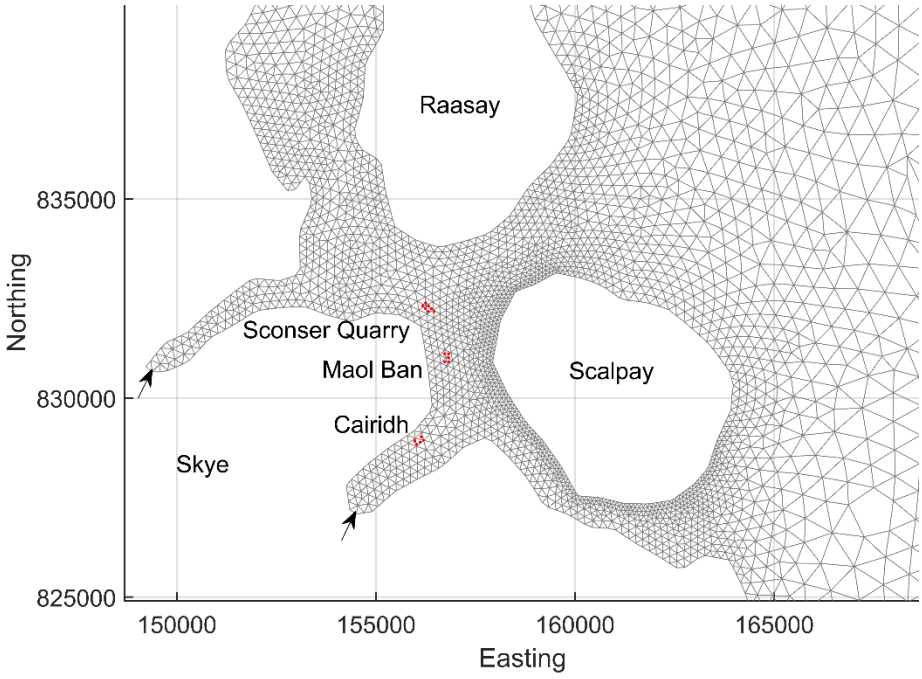

Figure 2. The unstructured mesh around the Caol Mor area containing three active Mowi farm sites (●): Caridh, Maol ban and Sconser Quarry. The modelled local river discharge locations are indicated (→).

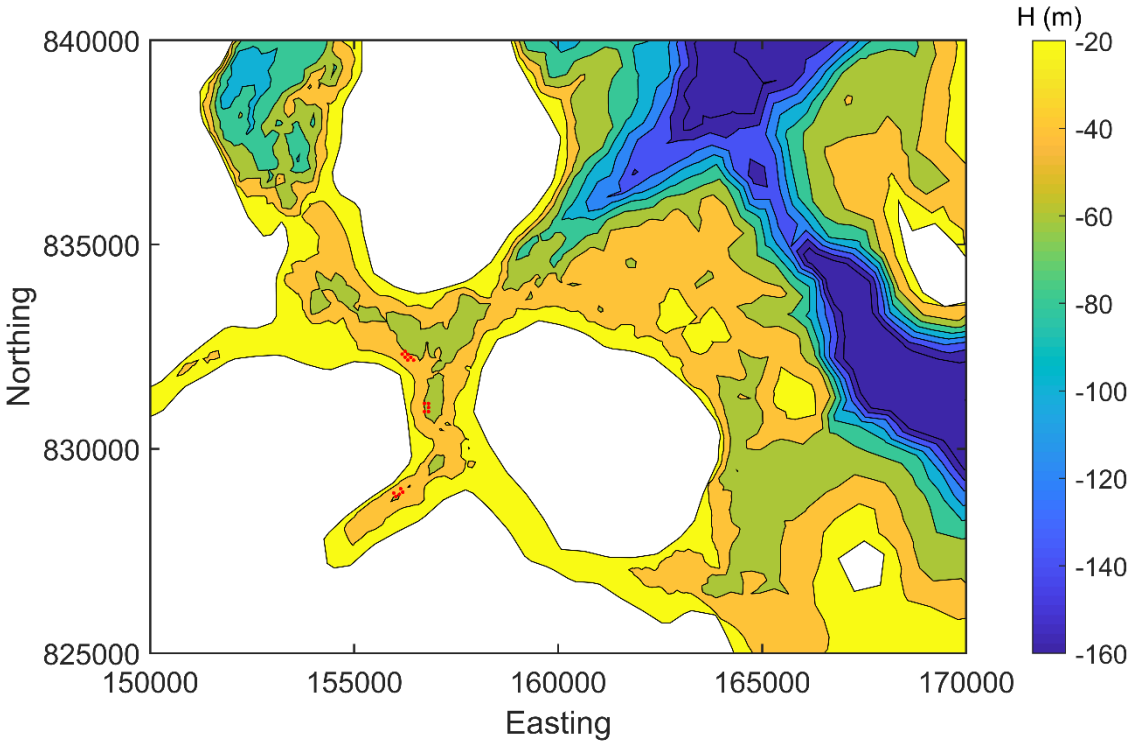

Figure 3. Model water depths, H (m), in the area around the Caol Mor salmon farms.

The model was forced along its open boundary by eight tidal constituents (O_1, K_1, Q_1, P_1, M_2, S_2, N_2, K_2), amplitudes and phase of which were obtained from the full Scottish Shelf Model. Spatially- and temporally-varying wind speed and direction data were taken from the ERA5 global reanalysis dataset for the required simulation periods (ECMWF, 2021), with the data converted to surface stress using Equation 6.

The model was run in 3D mode with 10 sigma layers evenly distributed over the water depth. Climatological river flow data, taken from the ECLH climatological runs (MS, 2016) were used. In all, 155 rivers are included in the ECLH domain, with two entering the domain in the Coal Mor region, with discharge locations into Loch Ainort and Loch Sligachan (Figure 2). The climatological seasonal cycle of daily river flows in these two rivers is shown in Figure 4.

In the vertical, a general length-scale (gls) turbulence closure scheme was used (Umlauf and Burchard, 2003; Warner et al., 2005). The closure scheme requires bed and surface roughness lengthscales to be specified; these parameters were refined during the calibration process.

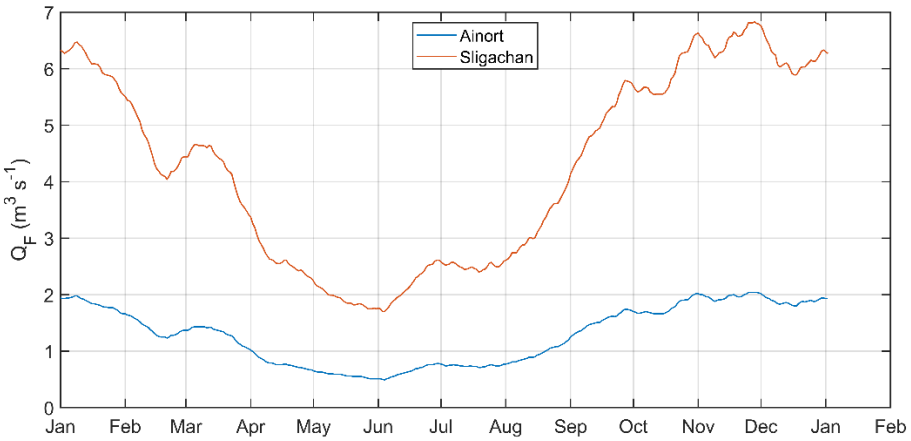

Figure 4. Annual climatological river flows into Loch Ainort and Loch Sligachan used in the modelling.

3. Model Calibration and Validation

The RiCOM model has previously been calibrated against sea level and current meter data from the north of Scotland (Gillibrand et al. 2016). For the current study, the model was further calibrated against hydrographic data collected in the Caol Mor region between 2016 – 2020. The data are described in the relevant hydrographic reports. In December 2016, an Acoustic Doppler Current Profiler (ADCP) was deployed at the Sconser Quarry site (ID132), and a second deployment took place from April – July 2020 (ID339). In July 2018, an ADCP was deployed close to the Maol Ban farm site (Figure 5) until September 2018 (ID230). A further deployment in the area was made at Cairidh from April – July 2020 (ID360). In all, 229 days of current data were used for calibration and validation in this application. ADCP deployments provided both current velocity and seabed pressure data, which were used to calibrate and validate modelled velocity and sea surface height. The model was calibrated initially against data from December 2016 – February 2017, then validated against the data from the three other deployments.

For each simulation, the model was “spun-up” for three days with boundary forcing ramped up from zero over a period of 48 hours. The model state at the end of the 72-hour spin-up period was stored, and the main simulations “hot-started” from this state.

The following main simulations were performed, corresponding with the dates of the ADCP deployments:

(i) Calibration: 5th December 2016 – 6th February 2017 (ID132)
(ii) Validation: 17th April – 8th July 2020 (ID339)
(iii) Validation: 5th July – 20th September 2018 (ID230)
(iv) Validation: 22nd September – 2nd December 2020 (ID360)

[Note that the dates above refer to the main simulations and that the spin-up simulations ran for three days prior to the start dates given above.]

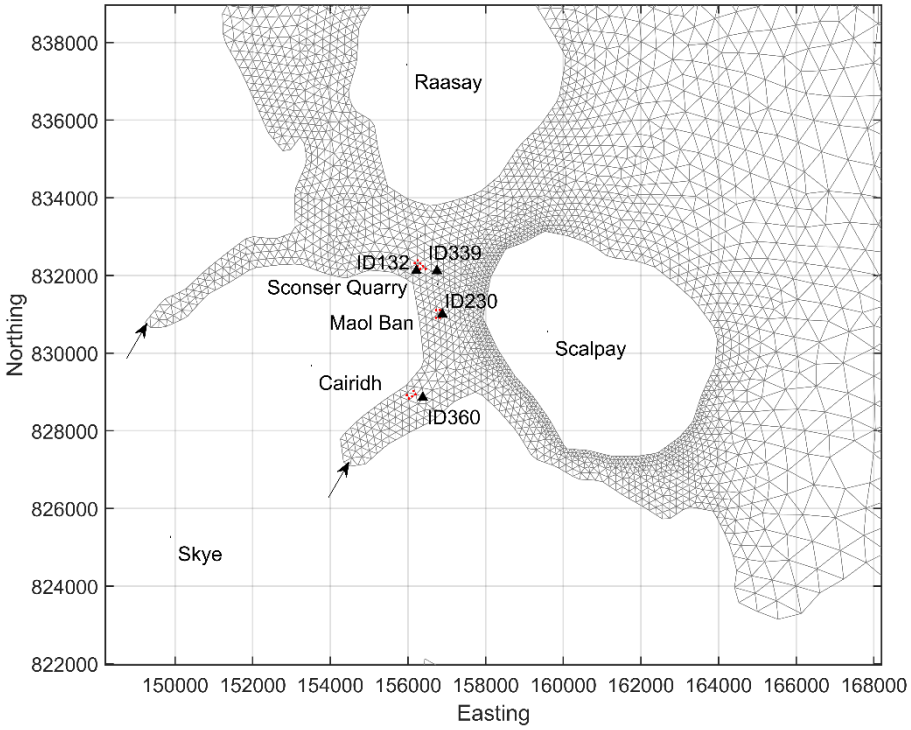

Figure 5. Locations of the ADCP deployments relative to the three farms at Caol Mor.

Model performance is assessed using three metrics: the mean absolute error (MAE), the root-mean-square error (RMSE) and the model skill (d_2). The first two are standard measures of model accuracy; the third, d_2, is taken from Willmott et al. (1985) and lies in the range $0 \leq d_2 \leq 1$, with $d_2 = 0$ implying zero model skill and $d_2 = 1$ indicating perfect skill.

3.1 Calibration: 5th December 2016 – 6th February 2017 (ID132)

The calibration used observed depth and current velocity from the ADCP location to compare with modelled sea surface height (SSH) and velocity (ADCP deployment ID132). The model was calibrated by varying the value of the bed and surface roughness lengthscales, z_0 and z_s. Simulations were performed with a range of values of both parameters, varying over the range $0.001 \leq z_0, z_s \leq 1.0$. After a number of simulations, a final parameter set was selected (Table 1).

Table 1. Parameter values chosen for the RiCOM model during the calibration simulations.

Parameter Description	Value
Bed roughness lengthscale, z_0 (m)	0.2
Surface roughness lengthscale, z_s (m)	0.2
Number of vertical layers	10
Model time step (s)	36.0

The results of the calibration exercise are presented in Figure 6 – Figure 9 and Table 2. At the ADCP location, the sea surface height was reasonably accurately modelled, with model skill of 0.99. The mean absolute error (MAE) and root-mean-square error (RMSE) values of 0.37 m and 0.44 respectively are about 7.5% and 8.8% of the spring tide range respectively.

For the calibration period, the model skill scores were 0.72 and 0.73 for the East and North components of near-surface (7m) velocity respectively, with RMSE values of 0.05 m s^{-1} and 0.04 m s^{-1} for the two components of velocity (Table 2). At the deeper depth of 17m, the skill scores were less good, at 0.58 and 0.63 respectively, but still reasonable given the challenges in calibrating hydrodynamic models against velocity data. The MAE and RMSE values were similar to the shallower depth. Given that bath medicine dispersion occurs primarily in the near-surface layer, we were most concerned with accurate representation of currents at 7m depth and placed most focus on those results.

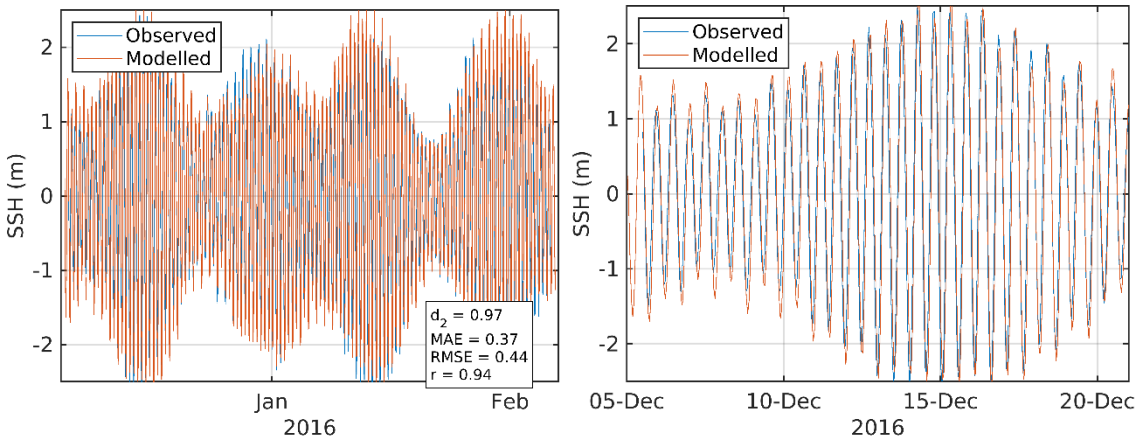

Figure 6. Comparison between observed and modelled sea surface height from December 2016 – February 2017 (ADCP deployment ID132) using model parameter values from Table 1. Both the full record (left) and a subset of 15 days (right) are shown. Observed data are in blue, model results in red.

Table 2. Model performance statistics for sea surface height (SSH) and East and North velocity at the ADCP location from December 2016 – February 2017 (ID132) at two depths (7m and 17m).

		Skill, d_2	MAE	RMSE
Sea Surface Height (SSH, m)		0.97	0.37	0.44
7m	East Velocity (m s^{-1})	0.72	0.05	0.07
	North Velocity (m s^{-1})	0.73	0.04	0.05
17m	East Velocity (m s^{-1})	0.58	0.05	0.06
	North Velocity (m s^{-1})	0.63	0.03	0.04

The scatter plots and histograms (Figure 8 and Figure 9) demonstrate that the modelled current had broadly the same magnitude and direction characteristics as the observed data. The deployment ID132 was located at the junction of three channels between Skye, Scalpay and Raasay, where dynamics are complex and challenging to simulate.

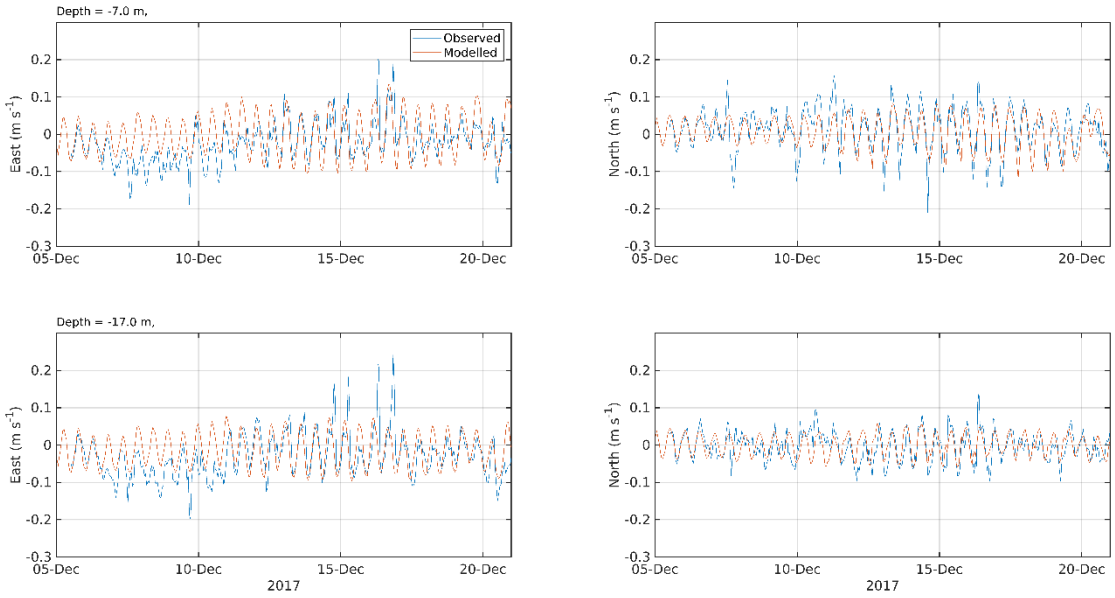

Figure 7. Comparison between observed and modelled East (left) and North (right) components of velocity at the ADCP location for 15 days in December 2016 – February 2017 (ID132) at two depths, 7m (top) and 17m (bottom). Observed data are in blue, model results in red.

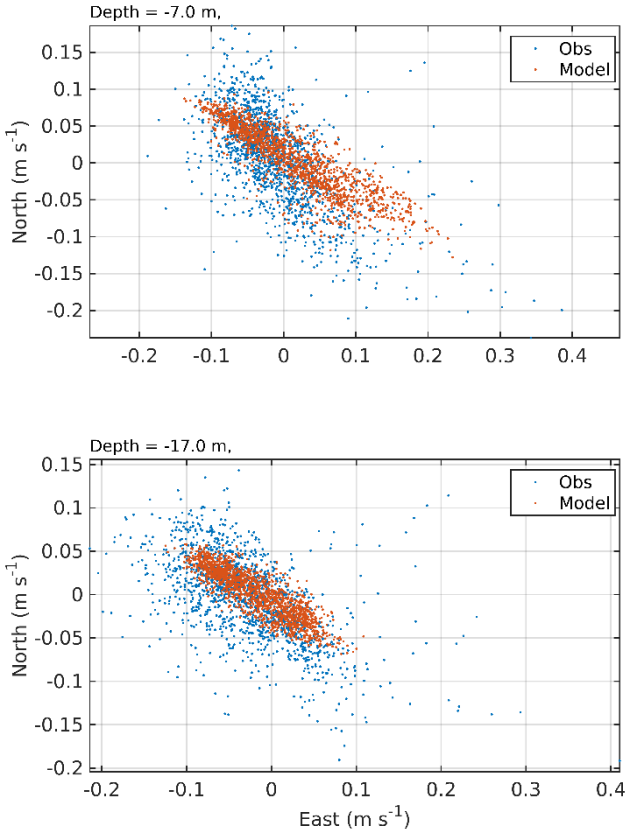

Figure 8. Scatter plot of observed and modelled velocity at the ADCP location from December 2016 – February 2017 (ID132) at two depths, 7m (top) and 17m (bottom). Observed data are in blue, model results in red.

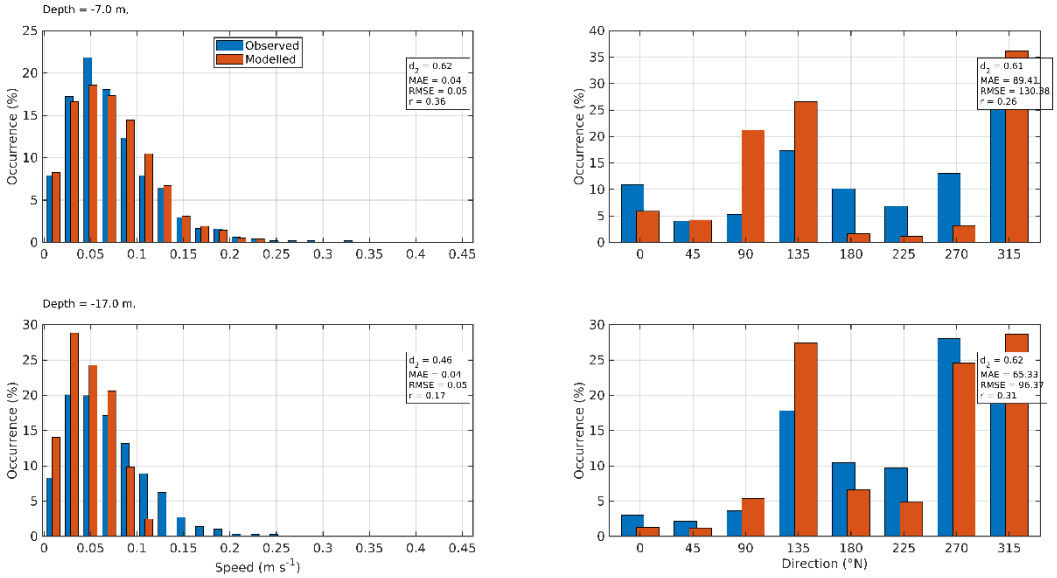

Figure 9. Histograms of observed and modelled speed (left) and direction (right) at the ADCP location from December 2016 – February 2017 (ID132) at two depths, 7m (top) and 17m (bottom). Observed data are in blue, model results in red.

3.2 Validation: 17th April – 8th July 2020 (ID339)

At the ADCP location, the sea surface height was reasonably modelled, with model skill of 0.96 (Figure 10, Table 3). The mean absolute error (MAE) and root-mean-square error (RMSE) values of 0.45 m and 0.52 respectively are about 9% and 10% of the spring tide range respectively.

Model skill scores were 0.52 and 0.80 for the East and North components of near-surface (7m) velocity respectively, with RMSE values of 0.04 m s^{-1} for both components of velocity (Figure 11, Table 3). The scatter plots and histograms shown in Figure 12 and Figure 13 demonstrate that the modelled currents were broadly of the same speed and direction as the observed data. The MAE and RMSE values were similar to the shallower depth.

Table 3. Model performance statistics for sea surface height (SSH), and East and North velocity at the ADCP location from April – July 2020 (ID339) at two depths, 6.9m and 16.9m.

		Skill, d_2	MAE	RMSE
Sea Surface Height (SSH, m)		0.96	0.45	0.52
6.9m	East Velocity (m s^{-1})	0.55	0.03	0.04
	North Velocity (m s^{-1})	0.78	0.03	0.04
16.9m	East Velocity (m s^{-1})	0.66	0.02	0.03
	North Velocity (m s^{-1})	0.83	0.03	0.03

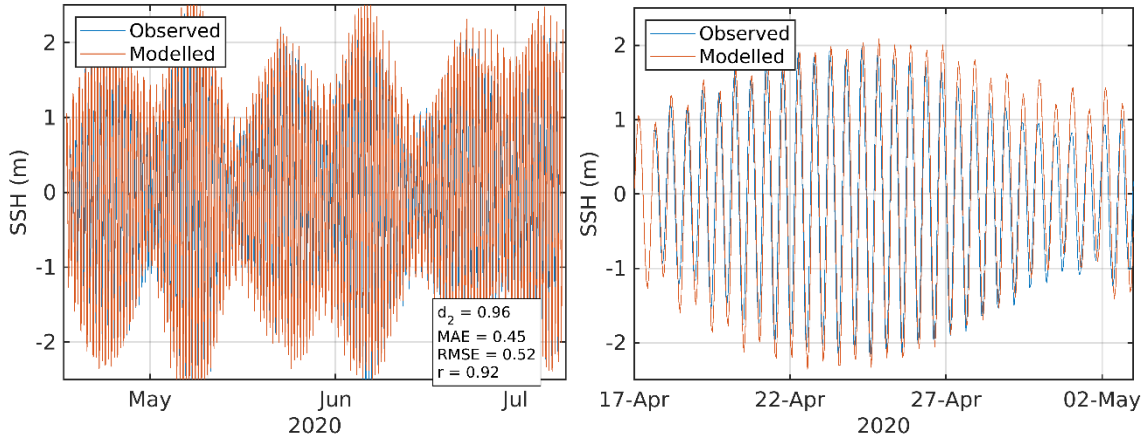

Figure 10. Comparison between observed and modelled sea surface height from April – July 2019 (ADCP deployment ID339) using model parameter values from Table 1. Both the full record (left) and a subset of 15 days (right) are shown. Observed data are in blue, model results in red.

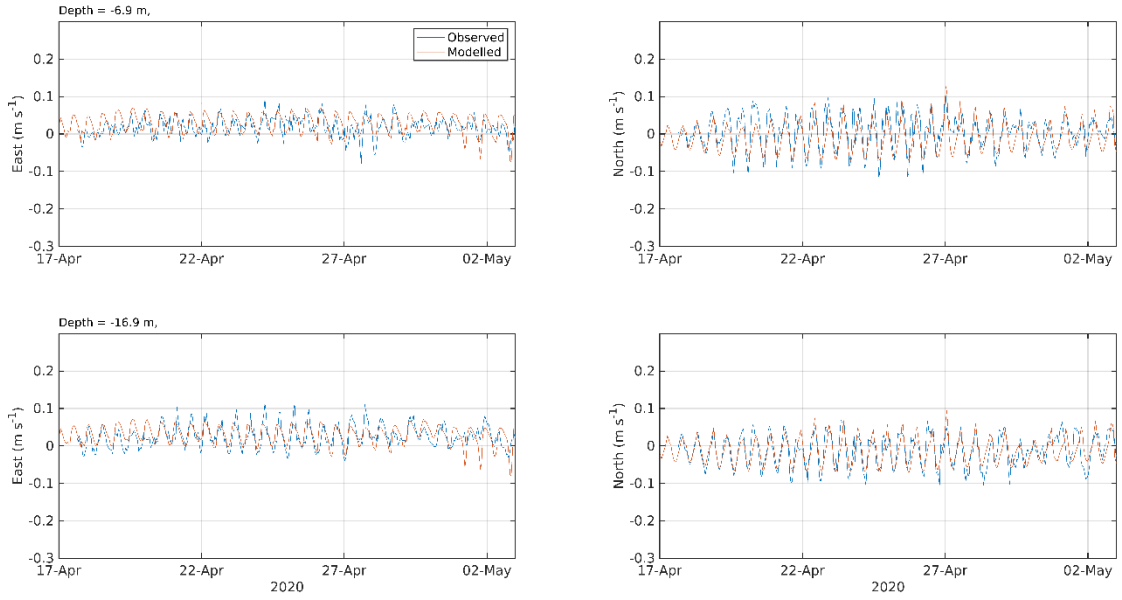

Figure 11. Comparison between observed and modelled East (left) and North (right) components of velocity at the ADCP location for 15 days in April – July 2020 (ID339) at two depths, 6.9 m (top) and 16.9 m (bottom). Observed data are in blue, model results in red.

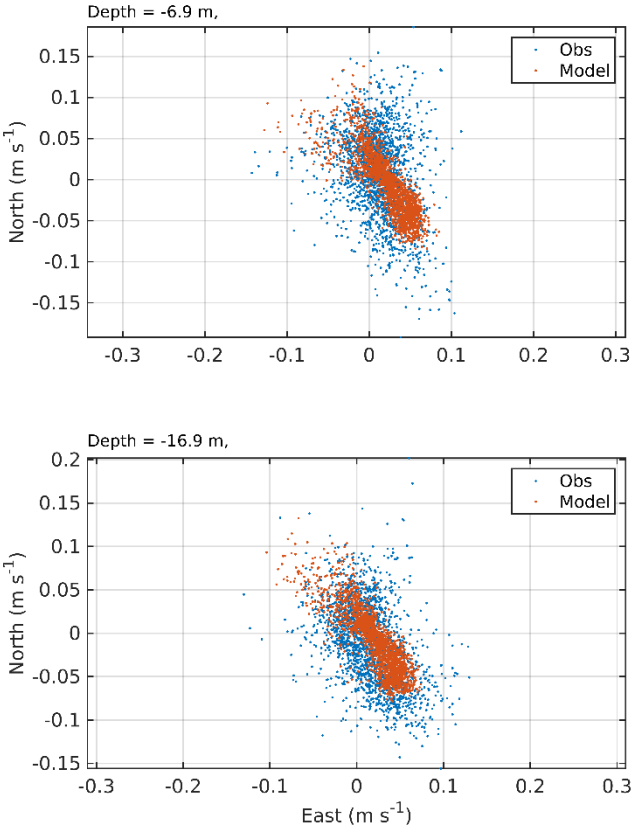

Figure 12. Scatter plot of observed and modelled velocity at the ADCP location from April – July 2020 (ID339) at two depths, 6.9m (top) and 16.9 m (bottom). Observed data are in blue, model results in red.

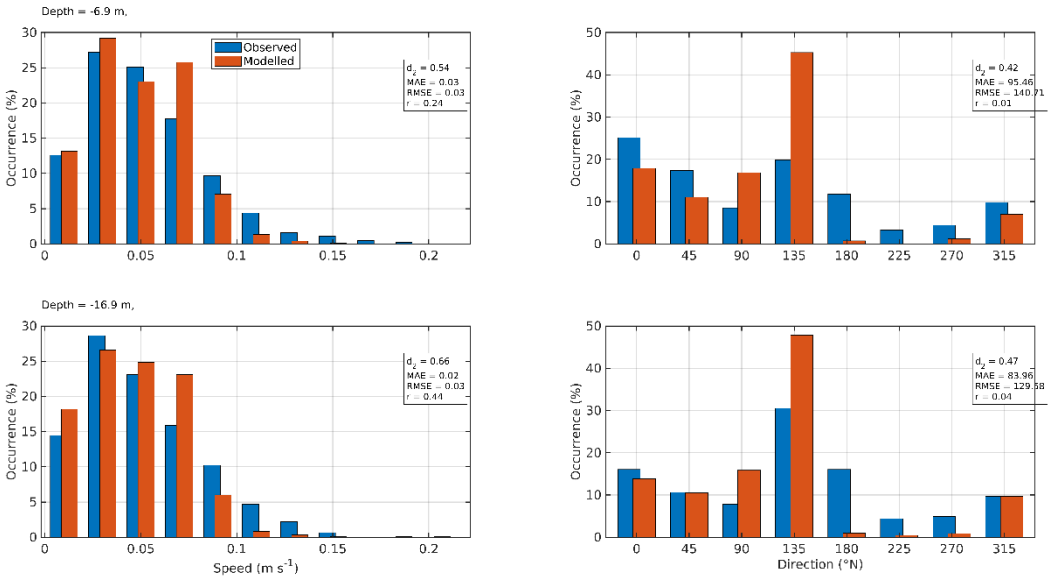

Figure 13. Histograms of observed and modelled current speed (left) and direction (right) at the ADCP location from April – July 2020 (ID339) at two depths, 6.9m and 16.9m (bottom). Observed data are in blue, model results in red.

3.3 Validation: 5th July – 20th September 2018 (ID230, Maol Ban)

At the ADCP location, the sea surface height was reasonably modelled, with model skill of 0.96 (Figure 14, Table 4). The mean absolute error (MAE) and root-mean-square error (RMSE) values of 0.38 m and 0.46 respectively are about 7% and 9% of the spring tide range respectively.

North and east components of near-surface (8.9m depth) velocity at the ADCP location were satisfactorily reproduced by the model, with values of the model skill, d_2, of 0.87 and 0.46 respectively (Figure 15, Table 4). The values of the MAE and RMSE were in the range 2 – 4 cm s^{-1} (Table 4). At the deeper depth (15.9 m), the model skill, RMSE and MAE values were similar. The scatter plots and histograms shown in Figure 16 and Figure 17 demonstrate that the modelled currents were broadly of the same speed and direction as the observed data.

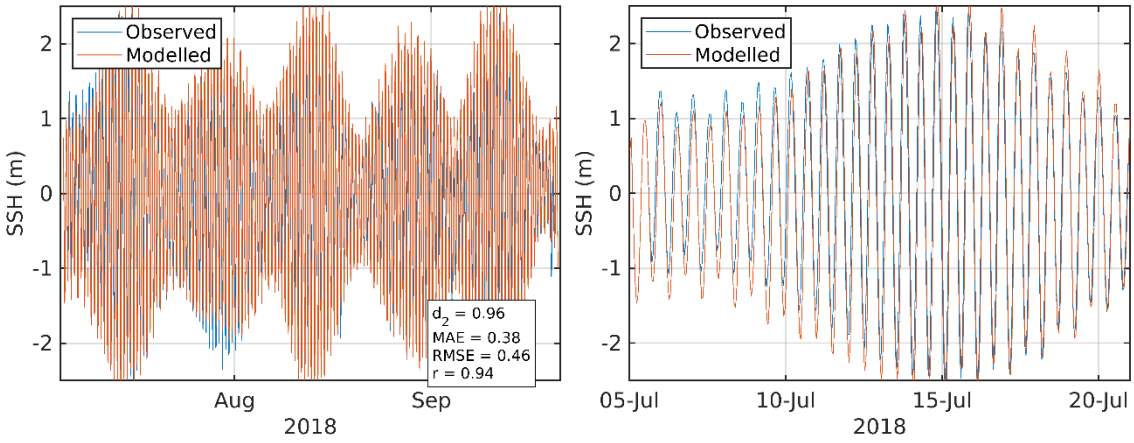

Figure 14. Comparison between observed and modelled sea surface height from July – September 2018 (ADCP deployment ID230) using model parameter values from Table 1. Both the full record (left) and a subset of 15 days (right) are shown. Observed data are in blue, model results in red.

Table 4. Model performance statistics for sea surface height (SSH), and East and North velocity at the Maol Ban ADCP location from the calibration simulation, July – September 2018 (ID230) at two depths, 8.9m and 15.9m.

		Skill, d_2	MAE	RMSE
Sea Surface Height (SSH, m)		0.96	0.38	0.46
8.9m	East Velocity (m s^{-1})	0.46	0.02	0.03
	North Velocity (m s^{-1})	0.87	0.03	0.04
15.9m	East Velocity (m s^{-1})	0.47	0.02	0.02
	North Velocity (m s^{-1})	0.80	0.03	0.04

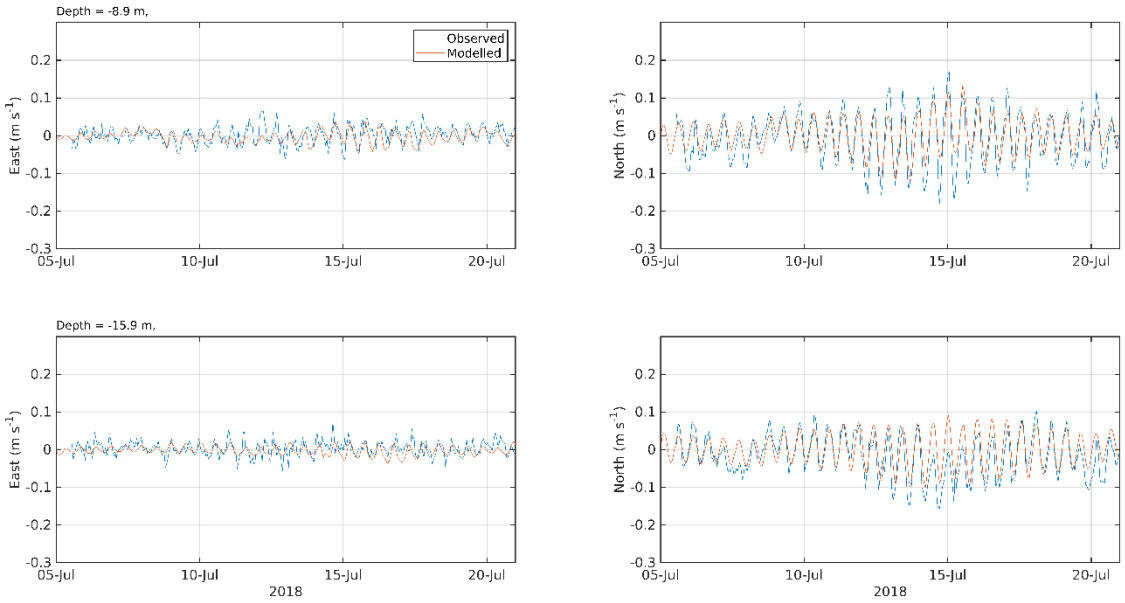

Figure 15. Comparison between observed and modelled East (left) and North (right) components of velocity at the ADCP location for 15 days in July 2018 (ID230) at two depths, 8.9m (top) and 15.9m (bottom). Observed data are in blue, model results in red.

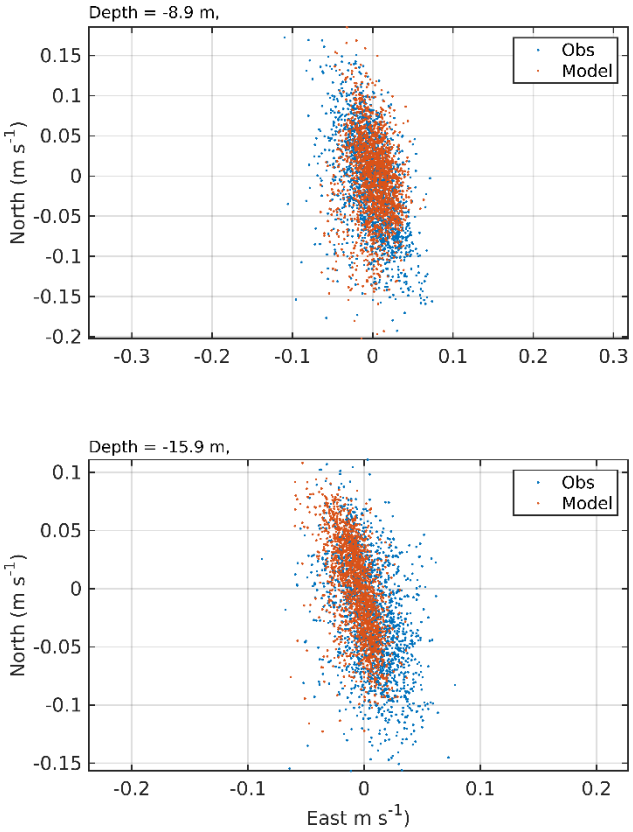

Figure 16. Scatter plot of observed and modelled velocity at the ADCP location from July – September 2018 (ID230) at two depths, 8.9m (top) and 15.9m (bottom). Observed data are in blue, model results in red.

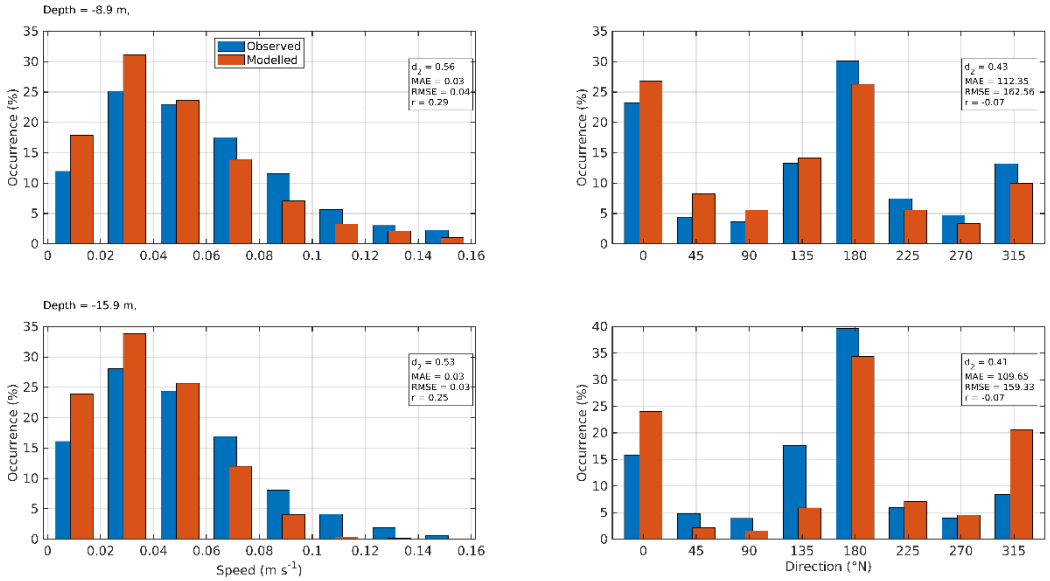

Figure 17. Histograms of observed and modelled current speed (left) and direction (right) at the ADCP location from July – September 2018 (ID230) at two depths, 8.9m (top) and 15.9m (bottom). Observed data are in blue, model results in red.

3.4 Validation: 22nd September – 2nd December 2020 (ID360, Cairidh)

At the ADCP location, the sea surface height was reasonably accurately modelled, with model skill of 0.98 (Figure 18, Table 5). The mean absolute error (MAE) and root-mean-square error (RMSE) values of 0.28 m and 0.35 respectively are about 5.5% and 7.0% of the spring tide range respectively.

North and east components of near-surface (5.9m depth) velocity at the ADCP location were satisfactorily reproduced by the model, with values of the model skill, d_2, of 0.57 and 0.56 respectively (Figure 19, Table 5), and values of MAE and RMSE being in the range 3 – 4 cm s^{-1} (Table 5). At the deeper cell (15.9 m), model skill for the North component of velocity was improved, while the East component was slightly worse. MAE and RMSE values were in the range 2 – 4 cm s^{-1}. The scatter plots and histograms shown in Figure 20 and Figure 21 demonstrate that the modelled currents were broadly of the same speed and direction as the observed data.

Table 5. Model performance statistics for sea surface height (SSH), and East and North velocity at the ADCP location from September – December 2020 (ID360) at two depths, 5.9m and 15.9m.

		Skill, d_2	MAE	RMSE
Sea Surface Height (SSH, m)		0.98	0.28	0.35
5.9m	East Velocity (m s^{-1})	0.57	0.03	0.04
	North Velocity (m s^{-1})	0.56	0.03	0.04
15.9m	East Velocity (m s^{-1})	0.50	0.03	0.03
	North Velocity (m s^{-1})	0.63	0.02	0.03

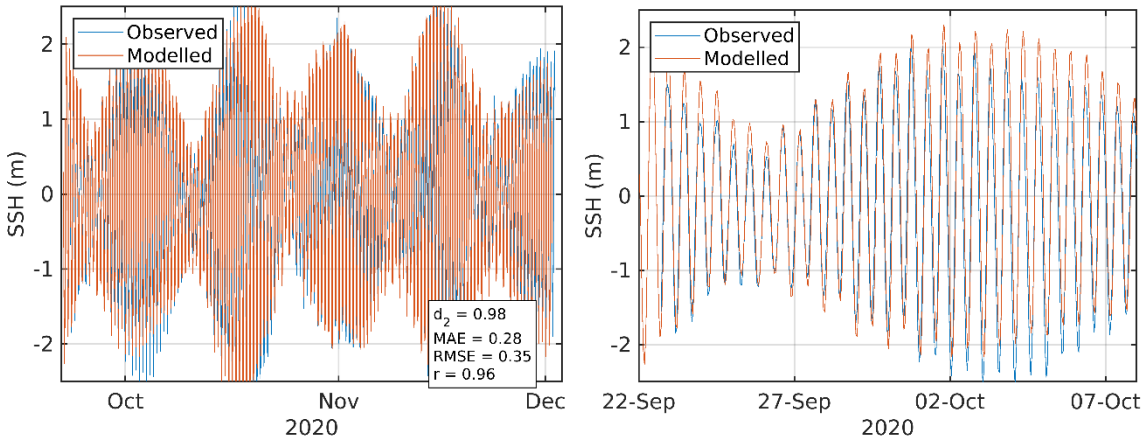

Figure 18. Comparison between observed and modelled sea surface height from September – December 2020 (ID360) using model parameter values from Table 1. Both the full record (left) and a subset of 15 days (right) are shown. Observed data are in blue, model results in red.

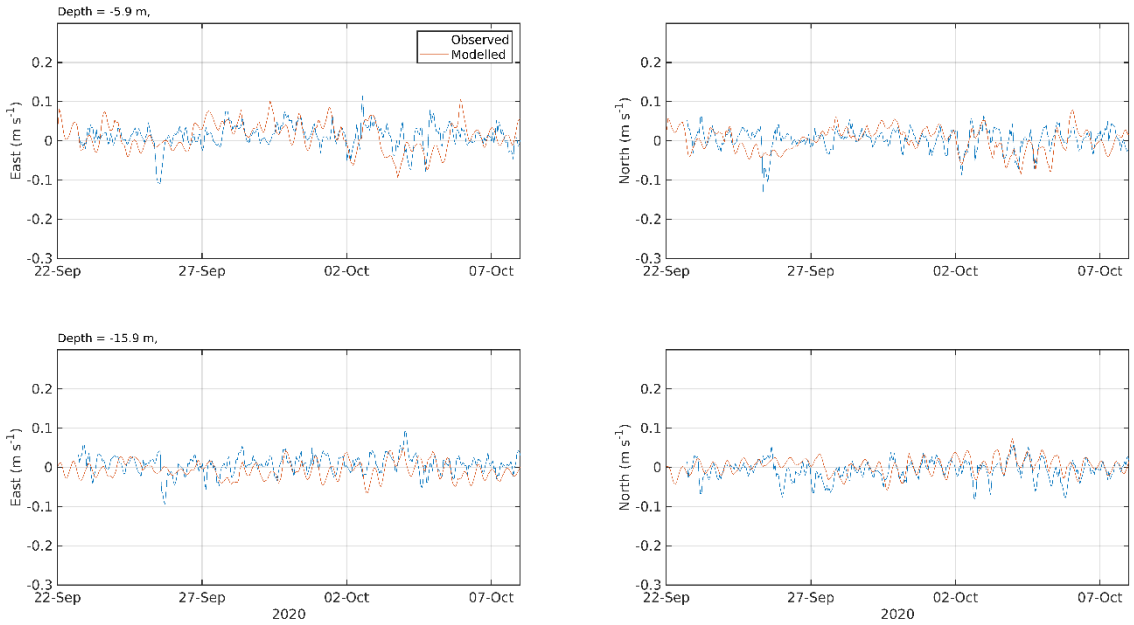

Figure 19. Comparison between observed and modelled East (left) and North (right) components of velocity at the ADCP location for 15 days in September – October 2020 (ID360) at two depths, 5.9m (top) and 15.9m (bottom). Observed data are in blue, model results in red.

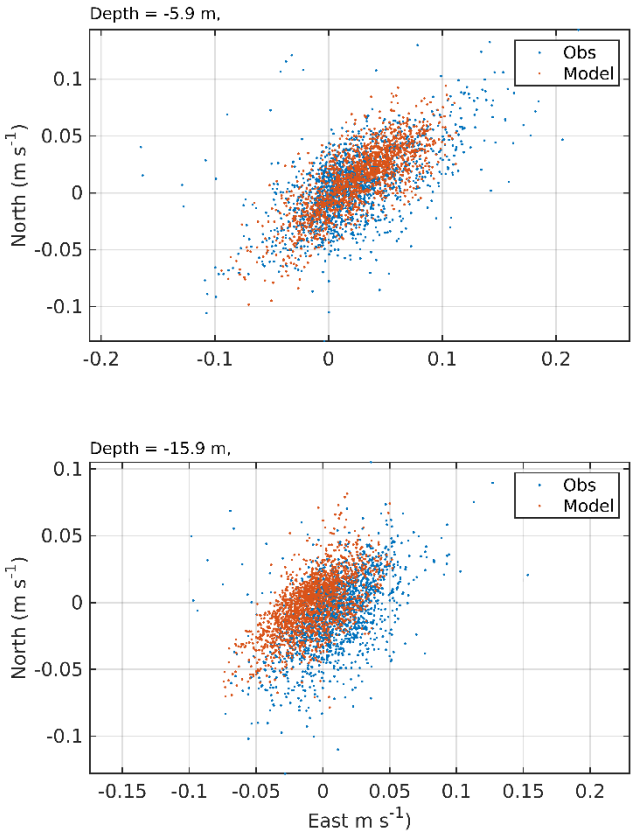

Figure 20. Scatter plot of observed and modelled velocity at the ADCP location from September – December 2020 (ID360). Observed data are in blue, model results in red.

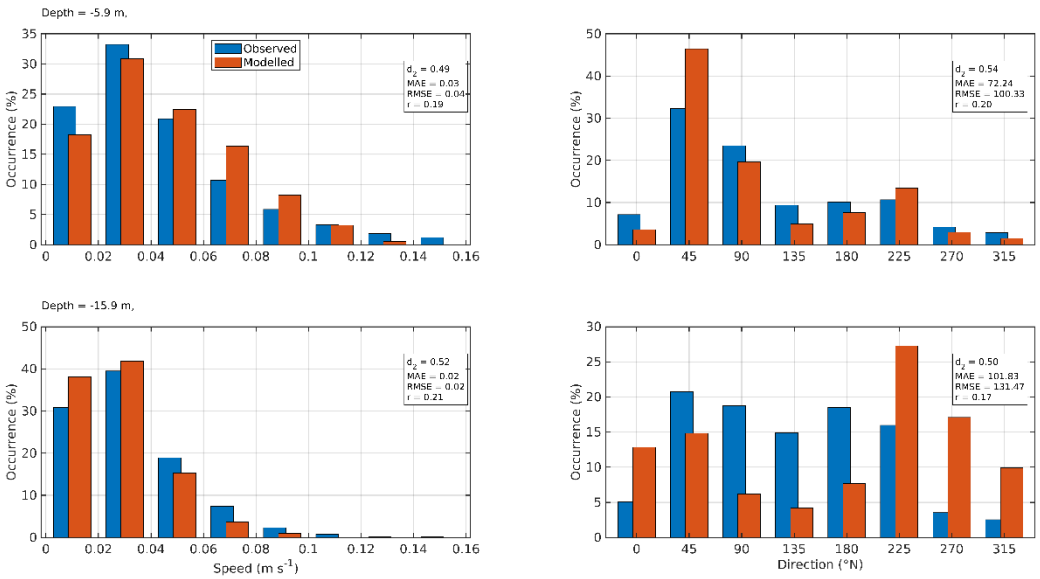

Figure 21. Histograms of observed and modelled speed (left) and direction (right) at the ADCP location from September – December 2020 (ID360) at two depths, 5.9m (top) and 15.9m (bottom). Observed data are in blue, model results in red.

4. Modelled Flow Fields

Modelled flood and ebb velocity vectors at spring tides are illustrated in Figure 22. Modelled current speeds in the Sound of Raasay at springs were typically 10 – 20 cm s^{-1}, but were weaker flowing around Scalpay and into Loch Ainort and Loch na Cairidh. Modelled currents speeds were weaker still during neap tides (Figure 23).

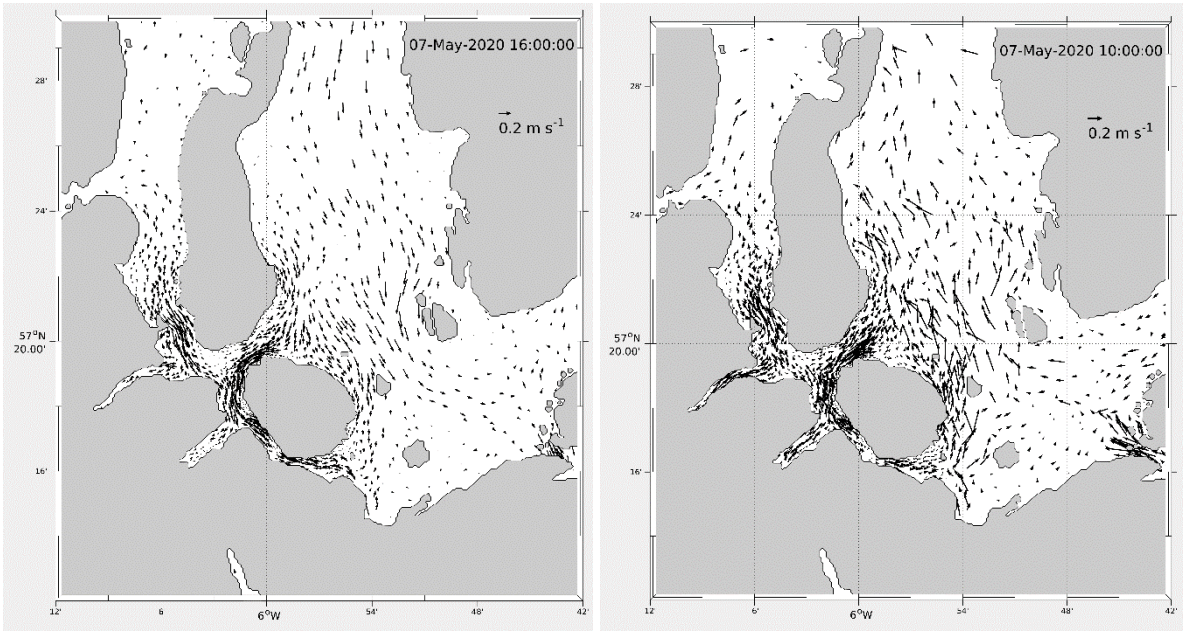

Figure 22. Modelled flood (left) and ebb (right) surface current vectors during spring tides on 7th May 2020. For clarity, only 25% of the model vectors are shown.

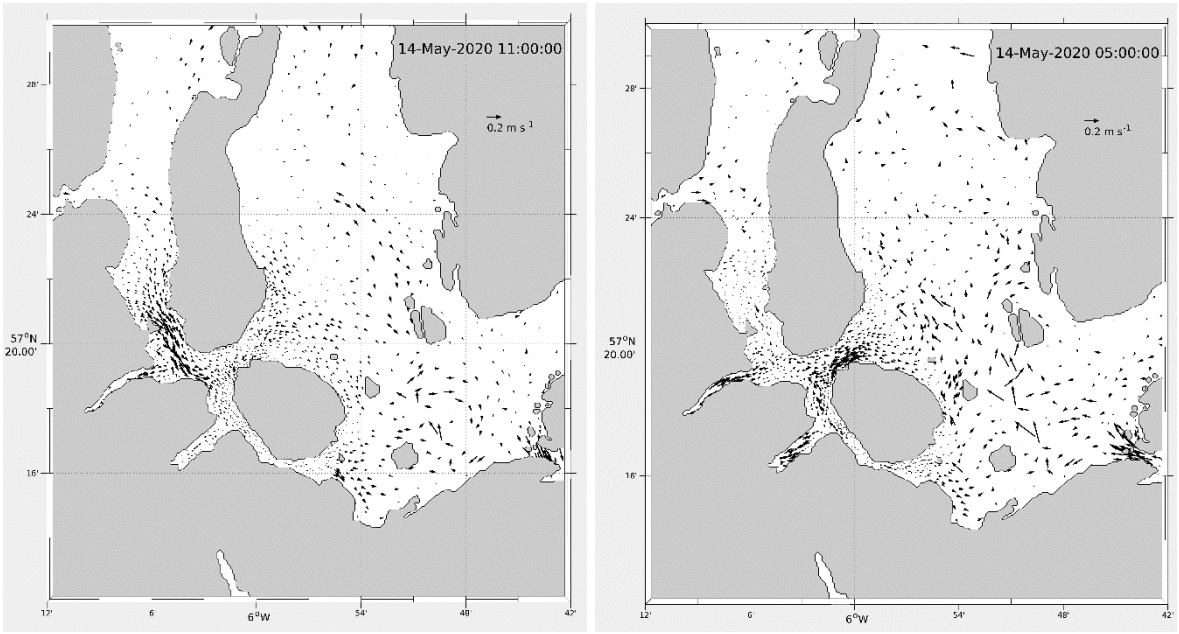

Figure 23. Modelled flood (left) and ebb (right) surface current vectors during neap tides on 14th May 2020. For clarity, only 25% of the model vectors are shown.

5. References

Casulli, V. 1987. Eulerian-lagrangian methods for hyperbolic and convection dominated parabolic problems. In: Taylor, C., Owen, D., Hinton, E. (Eds.), Computational Methods for Non-linear Problems, Pineridge Press, Swansea,U.K., pp. 239–268.

Edwards, A. and Sharples, F., 1986. Scottish Sea Lochs: A Catalogue. Scottish Marine Biological Association, Dunstaffnage Marine Laboratory, Oban, U.K., 400pp.

European Centre for Medium-Range Weather Forecasts (ECMWF) 2021, ERA5 Dataset https://www.ecmwf.int/en/forecasts/datasets/reanalysis-datasets/era5

Gillibrand, P.A.; Lane, E.M.; Walters, R.A.; Gorman, R.M. 2011. Forecasting extreme sea surface height and coastal inundation from tides, surge and wave setup. Austr. J. Civil Eng. 9, 99-112.

Gillibrand, P.A., Walters, R.A., and McIlvenny, J., 2016. Numerical simulations of the effects of a tidal turbine array on near-bed velocity and local bed shear stress. *Energies*, vol 9, no. 10, pp. 852. DOI: 10.3390/en9100852

Lane, E.M.; Gillibrand, P.A.; Arnold, J.R.; Walters, R.A. 2011. Tsunami inundation modeling with RiCOM. Austr. J. Civil Eng., 9, 83-98.

Large. W.G. and Pond, S., 1981. Open ocean momentum flux measurements in moderate to strong winds. J. Phys. Oceanogr., 11, 324—336.

Lewis, M., Neill, S.P., Robins, P., Hashemi, M.R., Ward, S., 2017. Characteristics of the velocity profile at tidal-stream energy sites. Renewable Energy, 114, 258-272.

Marine Scotland, 2016. Scottish Shelf Model. Part 4: East Coast of Lewis and Harris Sub-Domain. Available at https://www.gov.scot/publications/scottish-shelf-model-part-4-east-coast-lewis-harris-sub/pages/4/

McIlvenny, J. , Tamsett, D., Gillibrand, P.A. and Goddijn-Murphy, L., 2016. Sediment Dynamics in a Tidally Energetic Channel: The Inner Sound, Northern Scotland. Journal of Marine Science and Engineering, 4, 31; doi:10.3390/jmse4020031

Mowi Scotland Ltd. 2022, Sconser Quarry Bath Medicine Dispersion Modelling Report. January 2022, 32pp.

Plew, D. R.; Stevens, C. L. 2013. Numerical modelling of the effect of turbines on currents in a tidal channel–Tory Channel, New Zealand. Renew. Energy, 57, 269-282.

UKHO 2022, https://www.admiralty.co.uk/digital-services/data-solutions/admiralty-marine-data-portal

Umlauf, L.; Burchard, H. 2003. A generic length-scale equation for geophysical turbulence models, J. Mar. Res., 61, 235-265.

Walters, R. A. 2005a. Coastal ocean models: two useful finite element methods. Cont. Shelf Res., 25(7), 775-793.

Walters, R. A. 2005b. A semi-implicit finite element model for non-hydrostatic (dispersive) surface waves. Int. J. Num. Meth. Fluids, 49(7), 721-737.

Walters, R.A. 2016. A coastal ocean model with subgrid approximation. *Ocean Mod*., 102, 45-54.

Walters, R.A.; Casulli, V., 1998. A robust, finite element model for hydrostatic surface water flows. Comm. Num. Methods Eng., 14, 931–940.

Walters, R.A.; Gillibrand, P.A.; Bell, R.; Lane, E.M. 2010. A Study of Tides and Currents in Cook Strait, New Zealand. Ocean Dyn., 60, 1559-1580.

Walters, R.A., Lane, E.M., Hanert, E. 2009. Useful time-stepping methods for the Coriolis term in a shallow water model. *Ocean Model*., *28*, 66–74. doi: 10.1016/j. ocemod.20 08.10.0 04.

Walters, R.A. ; Lane, E.M.; Henry, R.F. 2008. Semi-lagrangian methods for a finite element coastal ocean model. *Ocean Model*., 19, 112–124.

Walters, R. A.; Tarbotton, M. R.; Hiles, C. E. 2013. Estimation of tidal power potential. Renew. Energy, 51, 255-262.

Warner, J.C.; Sherwood, C.R.; Arango, H.G.; Signell, R.P.; 2005. Performance of four turbulence closure models implemented using a generic length scale method. Ocean Modelling, 8, 81 – 113.

Willmott, C. J.; Ackleson, S. G.; Davis, R. E.; Feddema, J. J.; Klink, K. M.; Legates, D. R. O'Donnell, J.; Rowe, C. M. 1985. Statistics for evaluation and comparison of models, J. Geophys. Res., 90, 8995– 9005.

Wu, J. 1982. Wind-stress coefficients over sea surface from breeze to hurricane, J. Geophys. Res., 87(C12), 9704–9706, doi:10.1029/JC087iC12p09704.